

# ENA imaging simulation of the distant planetary magnetosphere and ENA emission discussion of the solar wind

Li Lu<sup>1,2,3</sup>, Qing-long Yu<sup>1,2,3</sup>, Shuai Jia<sup>1,2,3</sup>, Yuan Chang<sup>1,2,3,4</sup>

1. Laboratory of Space Environment Exploration, National Space Science Center of the Chinese Academy of Sciences, Beijing 100190, China
2. Beijing Key Laboratory of Space Environment Exploration, Beijing 100190, China
3. Key Laboratory of Science and Technology on Space Environment Situational Awareness, CAS, Beijing 101499, China
4. University of Chinese Academy of Sciences, Beijing 100049, China

**Key words** Energetic Neutral Atom (ENA), Image telemetry, Solar wind, Magnetosphere, Interplanetary Magnetic Field (IMF), heliosphere, heliopause, Planet

## Abstract

Whether the "ENA ribbon" image scanned remotely by IBEX-Hi at the lunar Resonance orbit really comes from the heliopause? It involves assessing the scale of solar wind particle loss throughout the solar system. The ENA imaging simulation results at the Lagrange point show that the scale of the planetary magnetosphere with a telemetry distance of AU magnitude is too small to contribute to "ENA ribbon". But the simulated effective ENA differential fluxes provide a reference for the physical scale evaluation of the huge magnetic structure in the heliopause. Near earth orbit, the ENA differential flux generated by the charge exchange between solar wind ions and local neutral gas is equivalent to the measurements of "ENA ribbon", which may be the main ENA emission source of the "ENA ribbon". If the ion flow of solar wind forms a tailward distribution loop under galactic wind pressure, the morphology difference of the ENA ribbon measured by IBEX-Hi between the Ram and anti-ram direction can be explained. 2D ENA imaging measurements at Lagrange points proposed here can be used to investigate the ENA ribbon origination by using the energy spectral lag vs disparity of ENA images.

## 1. Introduction

In 2009, the first ENA all-sky map of IBEX-Hi shows a bright ribbon of ENA emission believed to come from the edge of the heliosphere, where the local interstellar magnetic field interacting with the heliosphere [McComas et al., 2009; Puelier et al., 2009; Krimigis et al., 2009]. The IBEX maps reveal, superposed on a global ENA background, the enigmatic "ribbon" of enhanced ENA emission; it is up to ~3 times brighter than the background emission and spectrally distinct from it [McComas et al., 2011]. The ribbon appears as a continuous feature, it could be a string of more localized, overlapping "knots" of emission.

These ENA ribbon maps reveal distinct nonthermal (0.2 to 6 keV) heliosheath proton populations with spectral signatures ordered predominantly by ecliptic latitude, and the higher the energy, the higher the latitude [Funsten et al., 2009]. IBEX-Hi measured signals along the RAM direction of the Earth orbit are obviously stronger than the anti-RAM [McComas et al., 2012], and their enhancement is greater than the "purple shift" effect of energy spectrum caused by the earth's revolution speed. The ENA ribbon distribution patterns of the two all-sky maps are also different to some extent. Previous theories and numerical simulations could not predict the features of such ENA ribbon [Schwadron et al., 2009]. The ribbon's origin, whether inside or outside the heliopause or at more exotic locations in the local interstellar/interplanetary medium, is unknown.

Here, we summarize various hypotheses proposed before, simulate ENA imaging measurements

of the planetary magnetosphere, and discuss the possible sources of ENA emission signals in the "ENA ribbon" of planetary space.

## **2. Interplanetary/Interstellar ENA emission environment**

The solar wind is a stream of supersonic charged particles (mainly electrons and protons) constantly ejected from the outer layer of the solar atmosphere, including low speed ( $\sim 300$  km/s) and high speed ( $\sim 700$  km/s) [Bertaux et al., 1971]. The low speed solar wind originates from the helmeted coronal current, which mainly occurs near the ecliptic plane in low solar activity years and extends poleward in high solar activity years. The high-speed solar wind originates from coronal holes in the polar region [Fisk et al., 1974]. As the solar wind travels outward, it passes Mercury, Venus, Earth, Mars, Jupiter, Saturn, Uranus and Neptune in interplanetary space. Mercury, Earth, Jupiter, Saturn, Uranus and Neptune have internal magnetic fields that interact with the solar wind to form planetary magnetospheres. The size scale of these planetary magnetospheres depends on the strength of the magnetic dipole moment of the planet's internal magnetic field and the solar wind parameters around the planet's orbit.

During the solar activity, Mercury, which is closest to the sun, has strong coupling with solar wind disturbance. Because there is no obvious ionosphere and atmosphere, solar wind can directly reach the surface of the star through the polar cusp region and cause ion sputtering and escape. The earth's magnetosphere interacts with solar wind bow shock wave to pick up solar wind ions to form a ring current system, and then exchange charges with the neutral gas evaporating from the Earth to produce ENA emission, which can characterize the characteristics of ring current ions. At Jupiter and Saturn, the magnetic dipole moment is so strong that the magnetosphere is so large that the moons of the magnetosphere, such as IO and Enceladus, continue to emit plasma and dust, forming visible planetary ring systems. Uranus and Neptune are mainly characterized by large magnetic declinations of  $59^\circ$  and  $47^\circ$  respectively.

The Heliosphere can be regarded as the magnetosphere of the sun. Dialynas et al. [2006] and Wang et al. [2008] believed that the heliosphere was an immense magnetic bubble blown by the solar wind, where the local interstellar medium (LISM) are mostly neutral gas; Parent ions are pickup solar wind ions energized by the termination shock; The heliosheath's ENA emission (4~20 keV) has produced by charge exchange of those suprathermal ions with interstellar neutral atoms. In a graphical manner, McComas et al. [2010] illustrating the six possible sources of the ENA ribbon from outside as well as inside the heliopause, and suggested that: "The various possible mechanisms are not mutually exclusive, in fact, some combination or combinations may well ultimately explain the ribbon." To sum up: (1) Most ENA parent particles are been energized solar wind ions; (2) The pickup magnetic fields of energetic ions include the solar wind magnetic field, the interstellar medium magnetic field and the boundary magnetic field of the heliopause; (3) Neutral gas backgrounds for charge exchange are ubiquitous, independent of evaporative sources. The heliosphere /LISM interaction has been studied both theoretically and numerically for many years. Current heliospheric environmental properties have been inferred from remote sensing data and measurements of interstellar H, He and O atoms inside the heliosphere [Witte, 2004; Mobius et al., 2009]. Neutral gases in the earth's vicinity, unconstrained by magnetic fields, remain around the earth's orbit and are replenished annually. STEREO A and B orbit about 1 AU from the sun, and their measurements are representative of the interplanetary space environment, but the interstellar space environment [Luhmann et al., 2008]. Voyagers' in situ measurements across the heliopause are limited to two single points beside the ribbon, which are insufficient to provide

evidence that the magnetic field structure of the "immense magnetic bubble" at the heliopause, and the local interstellar medium (LISM) are mostly neutral gas.

Energy spectra of the ENA ribbon indicate that the ENA parent particle population is solar wind ions. The conditions under which these solar wind ions become measurable ENA emission sources are: (1) A magnetic field structure that can pick up solar wind ions and energizing them (i.e. a space for storing fluid), such as, interplanetary/interstellar magnetic fields, the magnetosphere of a planet. (2) A background neutral gas ( $\geq 10^6$  K) environment for the pickup ions ( $\sim$ keV) charge exchange in the fluid retaining space, such as, the neutral gas background environment formed by the planet's evaporated neutral atoms, or the ubiquitous interplanetary/interstellar neutral gas background. (3) Large scale ENA emission sources that meet the requirements of ENA imaging statistics, where "large scale" is relative to telemetry distances, such as solar wind ion flows in interplanetary space, AU magnitude distances in the planetary magnetosphere, or ENA emission walls supported by giant magnetic structures in the heliosphere beyond.

### 3. ENA imaging simulations of planetary magnetospheres

The time-difference of ENA energy spectrum and the parallax of ENA images collected in different energy channels contain the distance and location information of ENA emission source. When ENA signal transmission distance reaches a few AUs, the spectral time-difference can be count in days. Taking the energy channel dividing of IBEX-Hi as an example, time lags of hydrogen atoms traveling 1 AU at different energies are given in Table 1.

Table 1. The velocities and time lags of hydrogen atoms traveling 1 AU at different energies

E (KeV)	V (km/s)	T (hr)	$\Delta T$ (hr)
0.7	366.0509	113.5222264	22.962820341
1.1	458.8691	90.559406059	
1.7	570.4491	72.847087594	17.712318465
2.7	718.9097	57.803581668	15.043505926
4.3	907.2493	45.803899276	11.999682392

Usually ENA emission have event feature. Within the ecliptic plane, an Earth-size planet with a magnetosphere orbiting within the range of Jupiter (assuming an orbital radius of 7AU) is taken as an example, as shown in Figure 1: (1) At  $T_0$  ( $T_0=0$ ), the solar wind disturbance produces magnetic storm and ENA particle event with different energy at vernal equinox (the ecliptic longitude of the heliosphere  $\psi=0^\circ$ ); (2) At the time  $T_{4.3}$  ( $T_{4.3}=11$  days 11.19hr), the ENA imager collects ENA particles from Ram direction with energy  $E=4.3$ KeV at position A of the earth orbit, the observational longitude  $\alpha_{4.3}=187.8^\circ$ , and the ecliptic longitude of the heliosphere  $\psi_{4.3\text{keV}}=0.97^\circ$ , the X-axis points to the sun; (3) ENAs with energy  $E=1.7$ keV arrive at position B of the Earth orbit at the time  $T_{1.7}$  ( $T_{1.7}=18$  days 5.08hr) (from A to B, the payload has rotated about  $6.76^\circ$  along the Earth orbit at the ecliptic plane), and the observational longitude  $\alpha_{1.7}=180^\circ$ , the ecliptic longitude of the heliosphere  $\psi_{1.7\text{keV}}=0^\circ$ ; (4) At the time  $T_{0.7}$  ( $T_{0.7}=28$  days 11.21hr), the ENA imager collected ENAs with energy  $E=0.7$ keV from anti-ram direction at position C of the Earth orbit (from B to C, the payload rotated about  $10.17^\circ$  along the Earth orbit), the observational longitude  $\alpha_{0.7}=168.1^\circ$ , and the ecliptic longitude of the heliosphere  $\psi_{0.7\text{keV}}=-1.63^\circ$ . In the Figure 1,  $\psi_{0.7\text{keV}}$ ,  $\psi_{1.1\text{keV}}$ ,  $\psi_{1.7\text{keV}}$ ,  $\psi_{2.7\text{keV}}$  and  $\psi_{4.3\text{keV}}$  are the ENA image parallax generated by different energy ENAs with a same ENA event. Considering the continuity of the ENA spectrum, the result of observational ENA ribbon along the ecliptic longitude of the heliosphere is obtained.



images in the range of Jupiter and Saturn, as shown in Fig. 2.

Table 3. Position parameters of ENA imaging simulations

Scope	E (keV)	Latitude (°)	Longitude (°)	X (AU)	Y (AU)	Z (AU)
7 (AU)	0.7	90	-169.831	6.015708724	-0.176552213	0.0
	1.1	90	-175.632	6.002904555	-0.076162156	0.0
	1.7	90	180.00	6.0	0.0	0.0
	2.7	90	176.2900	6.00209566	0.064706476	0.0
	4.3	90	173.239	6.006954127	0.11772805	0.0
11 (AU)	0.7	90	-163.391	10.0417223	-0.285838896	0.0
	1.1	90	-172.721	10.00805905	-0.12670105	0.0
	1.7	90	180.00	10.0	0.0	0.0
	2.7	90	173.8180	10.00581516	0.107687028	0.0
	4.3	90	168.8864	10.01876114	0.192754885	0.0

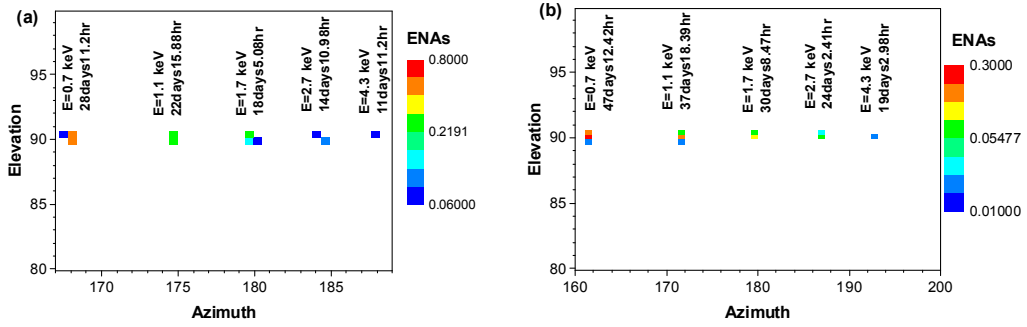


Fig. 2 Simulated ENA images of 1-day integral at the Lagrange point for magnetospheric planets with heliocentric distances of 7 AU (a) and 11 AU (b).

Table 4 shows the simulated detector azimuth and longitude of the heliospheric ecliptic caused by the time-delay phenomena of different energy channels. Considering the ENA event randomness and energy spectrum continuity, the point-like distribution of the simulated map is actually a ribbon formed by overlapping emission "nodes" along the longitude. The energy channels may overlap, and the length of overlap is related to the duration of the solar wind disturbance. The longitude distribution range of ENA ribbon images in different energy channels increases with the increase of telemetering distance, but the heliospheric ecliptic longitude disparity ( $\Delta\psi = \psi_{4.3\text{keV}} - \psi_{0.7\text{keV}}$ ) of ENA images in different energy channels decreases with the increase of telemetering distance. In the limit case, when ENA signal comes from the heliospheric top of 120 AU, the longitude disparity of ENA spectrum image decreases to 0 ( $\Delta\psi = 0$ ) theoretically. The ecliptic longitude of the peak flux of ENA ribbon in different energy channels increases with the increase of ENA energy, that is, it moves to the direction of earth revolution.

Table 4. FOV longitude simulation results for different energy channels

E (keV)	FOV azimuth (°)		Ecliptic longitude (°)	
	7 (AU)	11 (AU)	7 (AU)	11 (AU)
0.7	168.1	161.9	-1.63	-1.35
1.1	174.7	172.1	-0.72	-0.59
1.7	180.0	180.0	0.00	0.00
2.7	184.5	186.7	0.61	0.50

4.3	187.8	192.1	0.97	0.90
-----	-------	-------	------	------

The scale of the planetary magnetosphere is too small for AU magnitude telemetry distances that the solid angle toward a single detector is less than a pixel, and integral counts lasting one day cannot meet the statistical requirements of ENA imaging (Table 5). If we define an "effective differential flux" according to the actual solid angle of the planetary magnetosphere toward the detector, the simulation results of the average differential flux of the magnetosphere during a moderate magnetic storm ( $K_p=5$ ) in Table 5 are basically consistent with the actual measured results of the peak values of each IBEX-Hi channel [McComas et al., 2012].

Table 5. Simulation results of ENA counts and effective differential fluxes

E (keV)	ENA counts		Effective differential flux: ENAs/(cm <sup>2</sup> sr s keV)	
	7 (AU)	11 (AU)	7 (AU)	11 (AU)
0.7	0.8037	0.2991	941.9	978.2
1.1	0.3949	0.1366	294.5	298.3
1.7	0.3547	0.1279	171.1	171.4
2.7	0.1815	0.0661	55.1	55.7
4.3	0.1061	0.0397	24.2	21.0

Jupiter, located about 5.205 AU from the Sun, is the largest planet in the solar system and has a very large magnetic field, about 20,000 times stronger than Earth's at its source. Unlike Earth, Jupiter's magnetic field is generated not by its core, but by the interaction of elements in its outer core, which is made of liquid metal hydrogen. It is buffeted by solar wind, streams of charged particles, and magnetic fields constantly blowing from the sun. Depending on how strong the solar wind blows, Jupiter's magnetic field can extend out as much as 3.2 million kilometers (about 52 times farther than the Earth's magnetic field), with a magnetotail as far as Saturn's orbit (9.576 AU). The minimum solid Angle of Jupiter's magnetosphere to Lagrange point is about  $1.046 \times 10^{-4}$  ( $\sim 0.583^\circ \times 0.583^\circ$ ), which is larger than one pixel of ENA imager ( $0.5^\circ \times 0.5^\circ$ ). To obtain the differential flux measured as IBEX-Hi for Jupiter's distance, only one pixel ( $0.5^\circ \times 0.5^\circ$ ) in the Earth orbit, the number of solar wind energetic ions picked up by Jupiter's magnetosphere is  $\sim 2700$  times that of the Earth's magnetosphere during moderate storms. IBEX-Hi scans and imaging measurements in the vertical solar direction on the lunar resonant orbit [McComas et al., 2012] can collect ENA signals generated by Jupiter's huge magnetotail and obtain all-sky maps similar to the morphology of "ENA ribbon". Jupiter has several moons orbiting within its huge magnetic field, and the neutral gas evaporation and the effect on Jupiter's magnetic field will both contribute to ENA ribbons.

Saturn, about 9.576AU from the Sun, is the only planet whose magnetic field aligns with its axis of rotation. Saturn's magnetic field is 17 to 34 times stronger than Earth's and extends into Titan's orbit, making it the flattest shape. Due to the smaller size and far distance from Earth's orbit, the contribution to ENA ribbon emission should be small. Uranus and Neptune have magnetic fields 3-6 and 2-8 times that of Earth, respectively, and are further from Earth's orbit and the ENA emission contribution to ENA ribbon is negligible.

#### 4. ENA emission cones produced by intermittent solar wind currents near 1 AU

Based on the experience of ENA imaging measurements in the earth magnetosphere, we habitually choose spatially stable magnetic field structures to pick up solar wind ions to form ENA emission sources. Simulations show that the distant ( $\sim$ AU magnitude) source generating ENA ribbon

requires a large spatial magnetic field structure to generate enough ENA emission to meet the statistical requirements of particle imaging measurements. The results of the planetary magnetosphere simulation provide a reference for evaluating the physical scale of the giant ENA emission wall at the heliopause.

McComas et al. [2010] pointed out that the possibility of coexistence of multiple mechanisms was not excluded. They have suggested that ENAs come from shock accelerated pickup ions of solar wind inside the termination shock. The ENA emission of solar wind ions frozen in the interplanetary magnetic field (IMF) was considered to be optically thin before. The angle between the IMF (Archimedes spiral) and the radial diffusion speed of solar wind is the maximum pitch angle  $\alpha$  of solar wind ions. Near the Earth orbit, the solar wind ion, pitch angle  $\alpha \approx 45^\circ$ , exchanges charge with the neutral gas (density:  $N \sim 10^0 - 10^1 \text{ cm}^3$ ) evaporating from the earth corona to form a "ENA emission cone" with cone angle  $2\alpha \approx 90^\circ$ , as shown in Fig. 3.

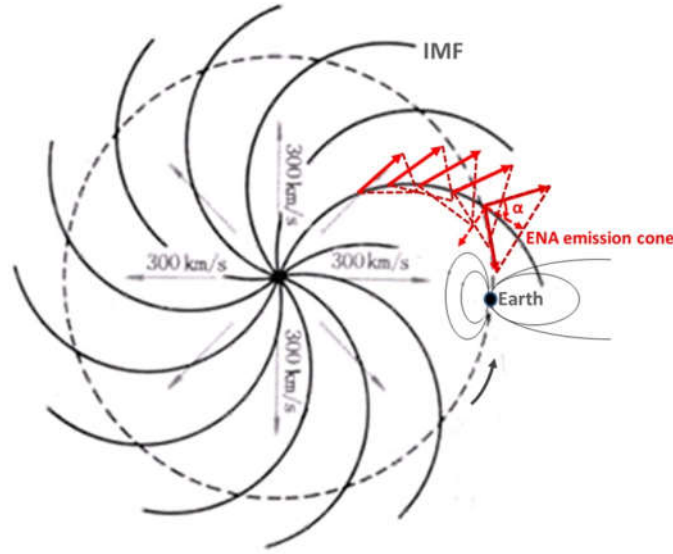


Fig. 3 The interplanetary magnetic field lines and the corresponding ENA emission cone (marked red) near 1 AU.

The IMF is a passive field, and the solar wind ion flow (energy spectrum  $\sim 1 \text{ keV}$ ) frozen in IMF near the Earth has intermittent emission characteristics. The Chang 'E-1 satellite traverses the solar wind ion stream in interplanetary space near the lunar orbit, lasting about a dozen minutes each time. The solar wind ion differential flux measured by solar wind ion detectors (SWID/A& B) is about  $10^6 - 10^7 \text{ cm}^{-2} \text{ sr}^{-1} \text{ s}^{-1} \text{ keV}^{-1}$ . It has obvious solar wind event contingency characteristics [Shi et al., 2014]. The differential flux of ENA emission:

$$\mathbf{J}_{\text{ENA}} = \mathbf{J}_p(\sigma_{\text{pH}}n_{\text{H}} + \sigma_{\text{pHe}}n_{\text{He}})\mathbf{L}$$

$\sigma_{\text{pH}} \sim 10^{-15} - 10^{-16} \text{ cm}^2$ . For IBEX-Hi measurements with ENA differential flux of  $10^1 - 10^2 \text{ cm}^{-2} \text{ sr}^{-1} \text{ s}^{-1} \text{ keV}^{-1}$ ,  $L \sim 10^4 - 10^5 \text{ km}$ . Considering the relative velocity of satellite and solar wind ( $\sim 10^2 \text{ km/s}$ ), the spatial scale of solar wind is similar to the estimated  $L$  value.

The differential flux maximum observed in ram direction of IBEX-Hi is about one times larger than that in the anti-ram direction [McComas et al., 2012], which is larger than the purple shift (or red shift) effect of the energy spectrum generated by the earth's revolution speed (29.8 km/s). The ENA ribbon distribution patterns of the two are also slightly different. If we consider the ENA emission cone contribution of solar winds and the neutral gas background (density:  $N \sim 10^{-1} - 10^0 \text{ cm}^3$ ) in interplanetary space, the ENA imager near the Lagrange point can observe this ENA

emissions from the ram direction perpendicular to the radial direction of the sun. The variation of solar wind ion energy with latitude also supports the measurement results of IBEX-Hi high energy segment [Funsten et al., 2009]. But in the anti-ram perpendicular to the sun's radial direction, IBEX-Hi is unable to receive signals from the ENA emission cone of the solar wind near Earth's orbit. As the radial distance extends outward, the pitch angle  $\alpha$  of solar wind ions will soon approach  $\leq 90^\circ$ , and the signal of ENA emission cone also has a chance to enter the anti-ram direction of IBEX-Hi.

"ENA ribbon" may correspond to a global distribution of solar wind ion flow. If the ion flow of solar wind forms a tailward distribution loop under galactic wind pressure, the ecliptic longitude distribution range of the anti-ram ENA ribbon at 1 AU distributed on the Mollweide projection map will be correspondingly reduced, as shown in Figure 17 of McComas et al., [2012]. The morphology variation between ram and anti-ram ENA ribbons may be caused by the variation of ENA emission radial distance.

## 5. Conclusion

we suspect that the magnetic structure of the heliopause pickup solar wind ions to form a huge ENA emission wall which enable measurements of ENA ribbon at distant Earth orbit, and believe the ENA emission cone of the solar wind in the interplanetary space is the main ENA emission source of the ENA ribbon. It is proposed that there exists a tailward solar wind ion current distribution loop in interplanetary space. The ENA differential flux generated by the "ENA emission cone" of the solar wind ion stream near 1 AU is of the same order of magnitude as the peak signal of the ENA ribbon.

By simulating ENA imaging of the magnetosphere of distant planets, we demonstrate how to measure the location of ENA emission sources using ENA signal parallax caused by energy spectrum delay. In the solar system, except for Jupiter, the magnetospheres of other planets are too small to meet the statistical requirements of ENA ribbon imaging. A single Jupiter, orbiting near the ecliptic, is not enough to produce the emission "knots" strung together in the ENA ribbon, especially to explain the sources of the high-latitude signals in the spectrum.

Lagrange points (L5, L4, or L3) within the plane of the Earth's orbit around the Sun, where the particle emission environment is clean, are ideal locations for the above measurements. The proposed 2D ENA imaging measurement can collect the time lag and disparity of peak ENA signals in different energy channels to confirm the spatial location of ENA emission sources and further investigate the origin of ENA ribbon. The azimuth variation of signals in 2D ENA image measured at Lagrange point (L5, L4, or L3), from ram to anti-ram direction, will be the key data support to identify the location of ENA emission source.

## Acknowledgements

This study was supported by the Strategic Priority Program (SPP) on Space Science Advanced Research of Space Science Issues and Payloads (No. XDA 15017100)

## References

- Bertaux J L, Blamont J E. Evidence for a source of an extraterrestrial hydrogen lyman-alpha emission[J]. *Astronomy and Astrophysics*, 1971, 11: 200-217
- Dialynas K, Krimigis S M, Mitchell D G, et al. The bubble-like shape of the heliosphere observed by Voyager and Cassini[J] *Nature Astronomy*, 2006, 1 (5): 0115.
- Fisk L A, Kozlovsky B, Ramaty R. An interpretation of the observed oxygen and nitrogen enhancements in low-energy cosmic rays[J]. *The Astrophysical Journal*, 1974, 190: L35-L37.



- Funsten H O, Allegrini F, Crew G B, et al., Structures and spectral variations of the outer heliosphere in IBEX energetic neutral atom maps [J]. *Science*, 2009, **326**: 964-966
- Krimigis S M, Mitchell D G, Roelof E C, et al., Imaging the intersection of the heliosphere with the interstellar medium from Saturn with Cassini [J]. *Science*, 2009, **326**: 971-973
- Lu L, Yu Q L, Zhou P, Zhang X, Zhang X G, Wang X Y, Chang Y, Simulation study of the energetic neutral atom (ENA) imaging monitoring of the geomagnetosphere on a lunar base [J]. *Solar-Terrestrial Physics*. 2021. Vol. 7, iss. 3. P. 3–10. DOI: 10.12737/stp-73202101.
- Luhmann J. G., Curtis D.W., Schroeder P., McCauley J., Lin R.P., Larson D.E., Bale S.D., Sauvaud J.-A., Aoustin C., Mewaldt R.A., Cummings A.C., Stone E.C., Davis A.J., Cook W.R., Kecman B., Wiedenbeck M.E., Rosengvinge T. von, Acuna M.H., Reichenthal L.S., Shuman S., Wortman K.A., Reames D.V., Mueller-Mellin R., Kunow H., Mason G.M., Walpole P., Korth A., Sanderson T.R., Russell C.T., Gosling J.T., STEREO IMPACT investigation goals, measurements, and data products overview [J]. *Space Sci Rev* (2008) **136**: 117–184 DOI 10.1007/s11214-007-9170-x
- McComas D J, Allegrini F, Bochsler P, et al., Global observations of the interstellar interaction from the Interstellar Boundary Explorer (IBEX) [J]. *Science*, 2009, **326**: 959-962
- McComas, D. J., et al. (2010), Evolving outer heliosphere: Large - scale stability and time variations observed by the Interstellar Boundary Explorer [J]. *J. Geophys. Res.*, **115**, A09113, doi:10.1029/2010JA015569
- McComas D J, Funsten H O, Puelier S A, et al., IBEX observations of heliospheric energetic neutral atoms: current understanding and future direction [J]. *Geophys. Res. Lett.*, 2011, **38**: L18101-L18109
- McComas D. J., Dayeh M. A., Allegrini F., Bzowski M., DeMajistre R., Fujiki K., Funsten H. O., Fuselier S. A., Gruntman M., Janzen P. H., Kubiak M. A., Kucharek H., Livadiotis G., Mobius E., Reisenfeld D. B., Reno M., Schwadron N. A., Sokół J. M., and Tokumaru M., The first three years of IBEX observations and our evolving heliosphere, [J]. *Astrophys. J. Supp.* 2012, **203**: 1-36, doi:10.1088/0067-0049/203/1/.
- Mobius E, Bochsler P, Bzowski M, et al., Direct observations of interstellar H, He, and O by the interstellar Boundary Explorer [J]. *Science*, 2009, **326**: 969-971
- Puelier S A, Allegrini F, Funsten H O, et al., Width and variation of the ENA flux ribbon observed by Interstellar Boundary Explorer [J]. *Science*, 2009, **326**: 962-964
- Schwadron N A, Bzowski M, Crew G B, et al., Comparison of Interstellar Boundary Explorer observations with 3D global heliospheric models [J]. *Science*, 2009, **326**: 966-968
- Shi Hong, Tian Li-Cheng, and Yang Sheng-Sheng, 2014. Analysis of data obtained by the solar wind ion detector onboard the Chang'E-1 Lunar orbiter [J]. *Acta Phys. Sin.* Vol. **63**, No. 6, p. 1-7, DOI: 10.7498/aps.63.069601.
- Stone E C, Cummings A C, McDonald F B, et al., 2013. Voyager 1 observes low-energy galactic cosmic rays in a region depleted of heliospheric ions. *Science*, 341 (6142): 150-153.
- Wang, L., Lin, R., Larson, D. et al. Domination of heliosheath pressure by shock-accelerated pickup ions from observations of neutral atoms [J]. *Nature* **454**, 81–83 (2008). <https://doi.org/10.1038/nature07068>
- Witte, M. (2004), Kinetic parameters of interstellar neutral helium. Review of results obtained during one solar cycle with the Ulysses/GAS - instrument, *Astron. Astrophys.*, **426**, 835–844, doi:10.1051/0004-6361:20035956.